

Design and Experimental Validation of Swirl Recovery Vanes for Propeller Propulsion Systems

Li, Qingxi; Öztürk, Kenan; Ragni, Daniele; Sinnige, Tomas; Eitelberg, Georg; Veldhuis, Leo; Yangang, Wang

DOI

[10.2514/1.J057113](https://doi.org/10.2514/1.J057113)

Publication date

2018

Document Version

Final published version

Published in

AIAA Journal: devoted to aerospace research and development

Citation (APA)

Li, Q., Öztürk, K., Ragni, D., Sinnige, T., Eitelberg, G., Veldhuis, L., & Yangang, W. (2018). Design and Experimental Validation of Swirl Recovery Vanes for Propeller Propulsion Systems. *AIAA Journal: devoted to aerospace research and development*, 56(12), 4719-4729. <https://doi.org/10.2514/1.J057113>

Important note

To cite this publication, please use the final published version (if applicable).
Please check the document version above.

Copyright

Other than for strictly personal use, it is not permitted to download, forward or distribute the text or part of it, without the consent of the author(s) and/or copyright holder(s), unless the work is under an open content license such as Creative Commons.

Takedown policy

Please contact us and provide details if you believe this document breaches copyrights.
We will remove access to the work immediately and investigate your claim.

Green Open Access added to TU Delft Institutional Repository

'You share, we take care!' – Taverne project

<https://www.openaccess.nl/en/you-share-we-take-care>

Otherwise as indicated in the copyright section: the publisher is the copyright holder of this work and the author uses the Dutch legislation to make this work public.



Design and Experimental Validation of Swirl-Recovery Vanes for Propeller Propulsion Systems

Qingxi Li,* Kenan Öztürk,† Tomas Sinnige,* Daniele Ragni,‡ Georg Eitelberg,§ and Leo Veldhuis¶
Delft University of Technology, 2629 HS Delft, The Netherlands
and
Yangang Wang**
Northwestern Polytechnical University, 710072 Xi'an, People's Republic of China

DOI: 10.2514/1.J057113

The momentum transferred to the fluid by a running propeller contains not only the desired axial component but also a rotational component that does not contribute to the propeller thrust. By introducing a set of swirl-recovery vanes (SRVs) downstream of the propeller, part of the rotational flow in the slipstream can be redirected into the streamwise direction, thereby producing extra thrust and enhancing the propulsive efficiency. The current study presents the development, application, and experimental validation of a low-order SRV design tool. The design method combines a short computational time with a detailed vane-shape representation. The procedure is presented together with a test example, consisting of a set of SRVs designed and manufactured for operation with a six-bladed propeller operating at thrust coefficient of $C_{T,P} = 0.32$. Results from the computations are subsequently validated by a wind-tunnel experiment with the propeller-SRV model. The SRVs were shown to provide extra thrust at all the considered propeller operating conditions. Because the installation of the SRVs does not lead to an increase in power consumption, it is thus shown that SRVs have the potential to increase the propulsive efficiency during all phases of the flight.

Nomenclature

C_d	= sectional drag coefficient; $d/(0.5\rho V^*2c)$
C_p	= pressure coefficient; $(p_s - p_\infty)/(0.5\rho V_\infty^2)$
$C_{T,P}$	= propeller thrust coefficient; $T_p/(\rho n^2 D^4)$
$C_{T,V}$	= SRVs thrust coefficient; $T_V/(\rho n^2 D^4)$
C_Q	= propeller torque coefficient; $Q/(\rho n^2 D^5)$
c	= chord length, m
c_r	= propeller blade root chord length, m
D	= propeller diameter, m
d	= sectional drag per unit span, N/m
F	= objective function of airfoil optimization process
h	= airfoil maximum camber, m
h_p	= airfoil maximum camber position, m
J	= propeller advance ratio; $V_\infty/(nD)$
M	= number of sections in SRV lifting line model
m	= index of section in SRV lifting line model
N	= vane count
n	= propeller rotation frequency, 1/s
p	= order of convergence in Richardson extrapolation
p_s	= static pressure, Pa
p_∞	= freestream static pressure, Pa
Q	= propeller torque, N · m

q	= grid refinement ratio in Richardson extrapolation
R	= propeller radius, m
R_{SRV}	= SRVs radius, m
r	= radial coordinate, m
T_p	= propeller thrust, N
T_V	= SRVs thrust, N
t	= airfoil maximum thickness, m
t_p	= chordwise position of maximum airfoil thickness, m
V_a, V_t	= axial and circumferential inflow velocities at SRV sections, m/s
V^*	= total inflow velocity at SRV sections; $\sqrt{(V_a + v_a)^2 + (V_t + v_t)^2}$, m/s
V_∞	= freestream velocity, m/s
v_a, v_t	= axial and circumferential induced velocities by SRVs, m/s
Z	= number of mesh points
z	= coordinate in axial direction, m
α	= angle of attack, deg
β	= pitch angle, deg
Γ	= circulation, m^2/s
Δr	= section span in SRV lifting line model, m
η	= propulsive efficiency; $((C_{T,P} + C_{T,V}) \cdot J)/(2\pi C_Q)$
ρ	= air density, kg/m^3
φ	= propeller phase angle, deg

Presented as Paper 2017-3571 at the 2017 AIAA AVIATION Forum, Denver, CO, 5–9 June 2017; received 15 January 2018; revision received 5 July 2018; accepted for publication 15 July 2018; published online 28 September 2018. Copyright © 2018 by the American Institute of Aeronautics and Astronautics, Inc. All rights reserved. All requests for copying and permission to reprint should be submitted to CCC at www.copyright.com; employ the ISSN 0001-1452 (print) or 1533-385X (online) to initiate your request. See also AIAA Rights and Permissions www.aiaa.org/randp.

*Ph.D. Candidate, Flight Performance and Propulsion Section, Faculty of Aerospace Engineering. Member AIAA.

†M.Sc. Student, Flight Performance and Propulsion Section, Faculty of Aerospace Engineering.

‡Assistant Professor, Wind Energy Section, Faculty of Aerospace Engineering. Member AIAA.

§Full Professor, Flight Performance and Propulsion Section, Faculty of Aerospace Engineering. Member AIAA.

¶Full Professor, Head of Flight Performance and Propulsion Section, Faculty of Aerospace Engineering. Member AIAA.

**Full Professor, School of Power and Energy. Member AIAA.

I. Introduction

AS EVIDENCED by the world's first aviation antipollution agreement and the new Airplane CO₂ Emissions Certification Standard approved by the United Nations agency Committee on Aviation Environmental Protection [1], fuel-efficient propulsion systems are urgently required to lower the emissions of commercial flights. Within this context, open rotors provide interesting opportunities because of their high propulsive efficiency. Among the most interesting design solutions, contrarotating open rotor (CROR) configurations are commonly considered as viable competitors to turbofan engines [2–6]. The creation of a rotational motion of the fluid by the first row of blades, expressed as a swirl component in the flow, is responsible for the energy lost in the fluid due to the torque of the propeller. The rotational motion does not result in any useful propulsive power but a decrease in propulsive efficiency. By recovering this contribution with the second row of blades, extra thrust can be produced

with a direct benefit on the propulsive efficiency. As illustrated by a technology-demonstration aircraft produced by Lockheed-Georgia, an 8% fuel saving and a 2.5% direct operating cost reduction were estimated for CROR engines compared with equivalent-technology-level turbofan engines [7]. By splitting the loading between two sets of blades, CROR exhibits a smaller radius than a single-rotation propeller with the same power loading, which makes it more appropriate for high-speed applications. Moreover, CROR configurations typically entail advantageous solutions for stability and control, including a considerable reduction of torque and gyroscopic loads, and enhanced aircraft flutter stability [2]. However, some inherent flaws of the CROR concept impose a restriction for broader application of this type of engine. Examples are the high weight of the propulsion system due to the complex gear system required for obtaining the contra rotation [8,9], together with additional interaction noise caused by the contra-rotating stage [10,11].

The swirl recovery can also be achieved by locating a set of stationary vanes behind a single-rotation propeller. This approach, where the blades of the second row are referred to as swirl-recovery vanes (SRVs), was proposed by NASA in the late 1980s [12]. As part of the Advanced Turboprop Project, SRVs were designed and tested at transonic cruise conditions. Experimental data showed an extra thrust of 2% at the design condition of the system [13], while no additional noise was observed [14]. Despite these promising results, the research on SRVs was stopped when the energy crisis ended in the 1990s.

Recently, the SRV concept was reintroduced by research groups at Delft University of Technology and Northwestern Polytechnical University. In the numerical SRV design process performed by Wang et al. [15] and Stokkermans et al. [16], the vane shape was parameterized and optimized. In both studies, a gradient-based optimization routine was coupled with an SRV analysis tool. In particular, a RANS-based simulation was used by Wang et al. [15] and lifting-line theory was applied by Stokkermans et al. [16]. The optimization results have shown extra thrust of the order of 2–5% from SRVs at relatively high propeller-loading conditions ($C_{T,p} = 0.45\text{--}0.55$). The unsteady interaction between the propeller and the SRVs was analyzed by Li et al. [17], and the main source of unsteadiness on the vanes was shown to be due to the rotor tip vortices. In the wind-tunnel tests conducted at DNW-LLF [18], particle-image-velocimetry (PIV) measurements confirmed a positive swirl recovery by the vanes, whereas a numerical study of the same configuration predicted an efficiency gain of 0.7%. In the same study, the tonal sound pressure levels were shown to be increased by 2–6 dB compared with the isolated propeller, even though the vanes were cropped to reduce vortex-interaction noise.

Despite previous focus on the understanding of the swirl-recovery mechanism, procedures for the parametric design of SRVs are not well developed. In the design work mentioned above, the design problem was set up by combining a blade analysis tool with an optimization routine. However, the results of optimization routines are susceptible to the definition of the initial point. Furthermore, a global optimum design can typically not be guaranteed, but only assumed after performing a series of optimizations with different initial design or by using a global optimization algorithm. Both approaches will lead to an increase in computational time [19], thus making them unsuitable for parametric design of SRVs. However, a variational design approach can be used to overcome these drawbacks. In this approach, as described by Hildebrand [20], an auxiliary function is formed, which includes both the objective function and the constraints multiplied by a Lagrange multiplier. By setting the partial derivatives of the auxiliary function to the design variables to zero, the objective function is minimized while respecting the constraints. As a result, the optimum is obtained without applying a dedicated optimization routine, thus reducing computational time. Such a method has been applied by Coney to design marine propellers with the optimum circulation distribution [21]. This approach can also be applied to the design of SRV by considering a radially nonuniform inflow condition, and it is appropriate for parametric study because the geometric details are not necessarily needed at the initial design stage.

This paper develops a hybrid framework for SRV design following a variational approach based on the optimum circulation distribution on the SRVs, which allows for a fast computation and optimization of the final vane shape. Before the design procedure, the flow around the isolated propeller is simulated by a RANS-based solver and given as input to the SRV design tool. The model is coupled with a low-fidelity lifting-line code to produce a relatively good prediction of blade forces, while maintaining the efficiency and feasible turn-around times for quick convergence of the optimal blade parameters. To allow for a subsequent validation of the design method, a set of SRVs was designed for a six-bladed propeller and tested in a low-speed wind tunnel. The measured propulsive performance of the SRVs is compared with the numerical predictions. The computed velocity profiles downstream of the propeller with and without SRVs installed are further validated by PIV measurements.

II. Design of the SRVs

A. SRV Design Procedure

The SRV design procedure was simplified into three steps as shown in Fig. 1. At the beginning of the procedure, the inflow conditions to the SRVs need to be determined. This can be done either experimentally by a wind-tunnel test, or numerically from a simulation of the isolated propeller as done in the current paper. In the second step, the optimal loading distribution on the SRVs is determined. The third step then constitutes an airfoil design routine to achieve the optimal loading distribution.

1. SRV Design Input from Numerical Simulation of the Isolated Propeller

Before the design of the SRVs, a description is required of the flowfield at the position of the SRVs. This was achieved by performing a numerical simulation of a given isolated propeller based on the Reynolds-averaged Navier–Stokes (RANS) equations. The propeller used in this research represents a scaled-model of a conventional propeller of a typical regional turboprop aircraft. It features six blades and a diameter of 0.406 m, as shown in Fig. 2. The hub of the propeller has a diameter of 0.084 m, and the blade pitch angle equals 30 deg at 70% of the radius.

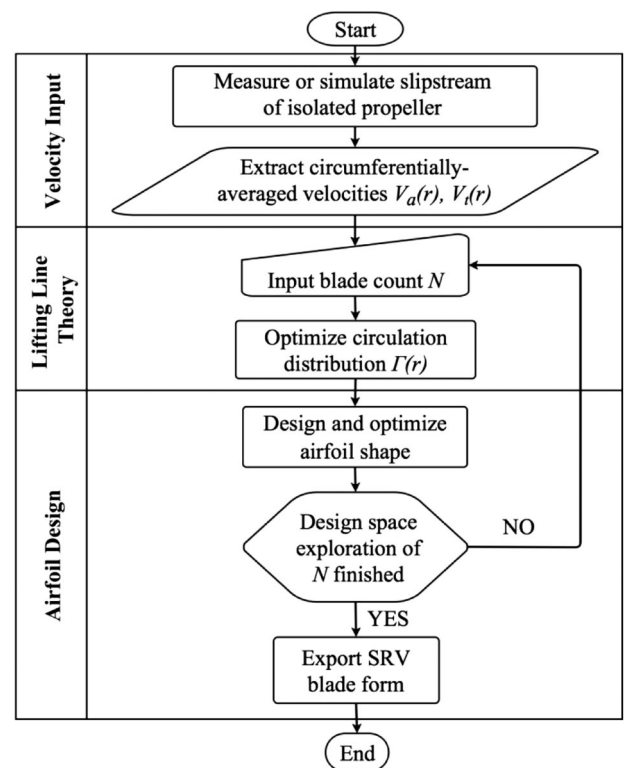


Fig. 1 Framework of the SRV design procedure.

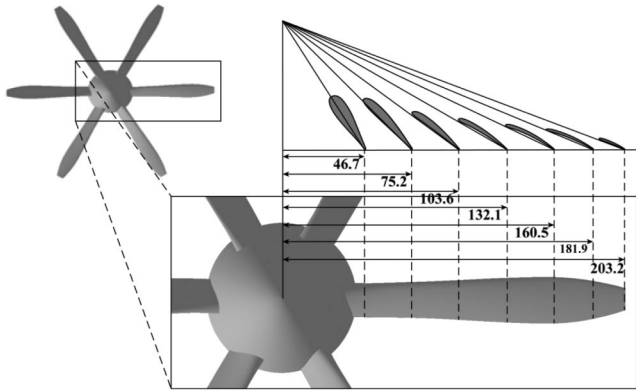


Fig. 2 Propeller layout (dimensions in millimeters).

The computational domain for the propeller calculation consisted of a cylinder extending about 10 times the propeller radius in all directions from the propeller-disk plane. This domain is larger than that was used in Ref. [22], which was already shown to be able to guarantee that the flowfield around the propeller blades was not perturbed by the boundary conditions. The mesh was generated by combining two separate blocks as shown in Fig. 3. For the cylindrical block surrounding the propeller (region I in Fig. 3a), a structured mesh was generated using NUMECA® Autogrid. Because of the symmetry of the propeller, only one blade sector of 60 deg needed to be meshed. The boundary layers around the blade and hub were resolved using 25 layers of hexahedron elements. For the second mesh block, an unstructured mesh was generated in ANSYS® ICEM. To ensure an adequate resolution of the propeller slipstream at the position of the SRVs, smaller tetrahedral elements were arranged in a cylindrical area downstream of the propeller block (region II-1 in Fig. 3a).

The inlet of the domain was modeled as a velocity inlet, with a turbulence intensity of 5%. Combined with a relatively high eddy viscosity ratio (the ratio between the turbulent viscosity and the molecular dynamic viscosity equals 10), this resulted in a turbulence level at the propeller plane equal to the level of 0.5% characteristic [23] of the wind tunnel used for the validation experiment (discussed in Sec. III.A). At the outlet of the domain, the average static pressure was prescribed to be equal to the undisturbed static pressure. The SRV fairing, which was required to house the instrumentation of the SRVs in the validation experiment, was modeled with a no-slip wall boundary condition. In contrast, the nacelle behind the SRV fairing, which extends further downstream to the outlet, was modeled as a free-slip wall to reduce the number of grid points. On the sides of the computational domain, periodic boundary conditions were specified. The conservation equations were solved based on a rotating reference frame, and an alternate rotation model was used for the advection term in the momentum equation.

The shear stress transport (SST) turbulence model, which gives good prediction of adverse pressure gradient flows (e.g., in the propeller studies of Refs. [24,25]), was used together with an

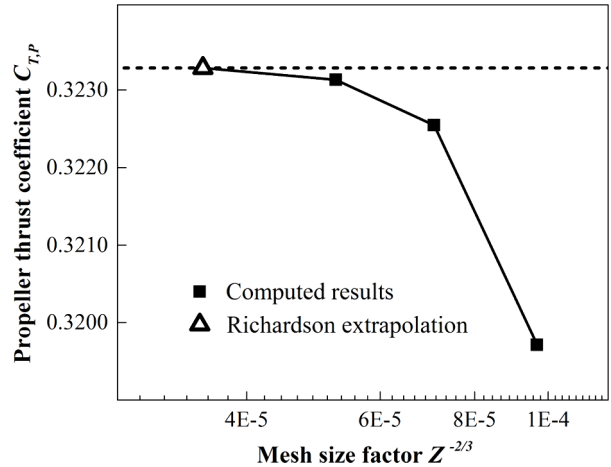


Fig. 4 Result of the mesh refinement study showing the propeller thrust coefficient as function of the mesh size factor Z .

automatic wall function. The simulation was performed at a freestream velocity of 29 m/s, which was equal to the maximum value attainable in the wind tunnel used for the validation experiment. The corresponding Reynolds number based on freestream velocity and propeller diameter was 7.9×10^5 . A high loading condition of the propeller, which corresponds to a typical take-off setting, was chosen as the design point to compensate for the low freestream dynamic pressure, thus obtaining a measurable thrust on each vane. The selected operating point corresponded to a computed propeller thrust coefficient of 0.322.

A grid refinement study was carried out on three meshes: coarse ($y^+ = 4$, $Z = 1.05$ million), medium ($y^+ = 2$, $Z = 1.68$ million), and fine ($y^+ = 1$, $Z = 2.63$ million). The propeller thrust coefficient is plotted in Fig. 4 with respect to the mesh size factor ($Z^{-2/3}$). As the mesh size reduces, the propeller thrust coefficient approaches an asymptotic value of $C_{T,P} = 0.3233$. This value was obtained by applying Richardson's rule [26] using the predictions of the medium and fine meshes, with a refinement ratio $q = 2$ and order of convergence $p = 2.27$.

To verify asymptotic convergence of the tested meshes, the grid convergence index (GCI) was determined for both the medium and fine meshes. A percentage of $GCI_{\text{fine,medium}} = 0.14\%$ was achieved with the fine mesh and $GCI_{\text{medium,coarse}} = 0.69\%$ with the medium mesh. When comparing these two values by:

$$\frac{GCI_{\text{fine,medium}}}{GCI_{\text{medium,coarse}}} \cdot q^p = 1.0018 \quad (1)$$

the ratio is approximately one which indicates that the solutions are well within the asymptotic range of convergence.

The radial distributions of the circumferentially-averaged axial velocity, V_a , and tangential velocity, V_t , are critical input information

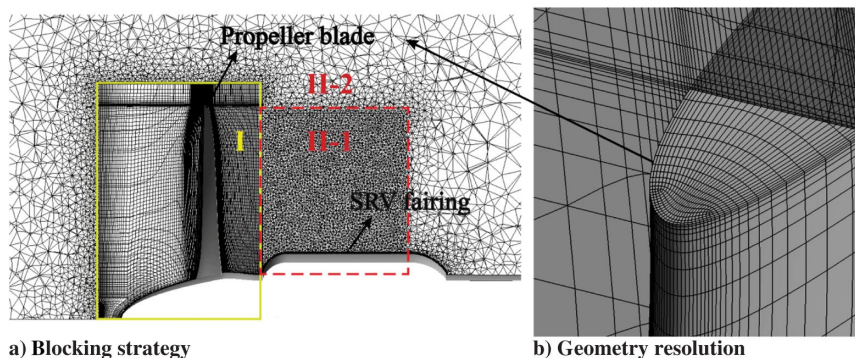


Fig. 3 Hybrid computation mesh for the isolated propeller.

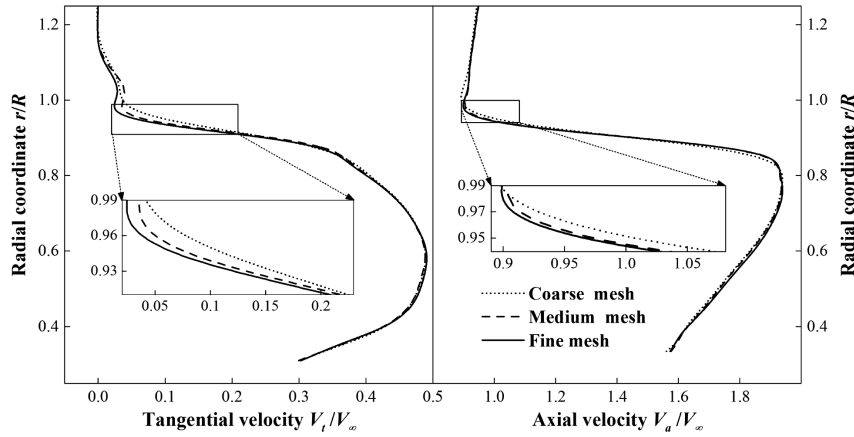


Fig. 5 Comparison of computed circumferentially averaged tangential and axial velocity distributions from different meshes at $J = 0.6$.

for the SRV design. The results obtained using the three meshes are compared in Fig. 5. A survey plane was located at the SRV midchord position at $3.75c_r$ downstream of the propeller. A maximum difference of 0.36 m/s (1.2% of the freestream velocity) was observed for the tangential velocity when comparing the results obtained with the medium and the fine meshes. For the axial velocity, the maximum difference was 0.27 m/s (0.9% of the freestream velocity), occurring in the blade tip region. The reason why the computed velocities from the coarse mesh differ more from the other two meshes is the larger element size in the slipstream. In the simulation with the coarse mesh, the blade tip vortex is more spread out compared with the results obtained with the medium and fine meshes, leading to a slower decay of both the axial and the tangential velocities toward the outer undisturbed flow.

The axial and tangential velocity distributions from the CFD simulation are taken directly as the inflow condition for the SRV design, based on the assumption that the upstream effect of the SRVs on the time-averaged propeller performance is negligible. This was confirmed by the propeller-loading measurements and the pressure measurement behind the propeller, as discussed later in Sec. III.D, and has also been shown in previous work [18].

2. Determination of Optimal Circulation Distribution on the SRVs

The optimal circulation distribution on the SRVs was obtained with a model based on lifting-line theory as developed by Epps and Kimball [27]. In this theory, the N vanes are simplified into N lifting lines with equal angular spacing and identical loading. Sweep and lean are not included in the current design method. The wake model of the vanes consists of constant-pitch, constant-radius helical vortices, the direction of which is aligned with the total velocity V^* at the vane position including the induced velocities. The thrust of the SRVs comes from the axial component of the lift and drag acting on the vanes. The Kutta–Joukowski (K–J) theorem is applied to determine the local lift on each vane section. By applying the K–J theorem, two main assumptions are made: first, the radial component of the slipstream velocity is neglected such that the flow surrounding the vane is two-dimensional (2D) on each radial section; second, each 2D section has a uniformly distributed inflow of V^* . The thrust generated by the SRVs can then be expressed as:

$$T_V = \rho N \sum_{m=1}^M \left((V_{t_m} + v_{t_m}) \Gamma_m - \frac{1}{2} V_m^* C_{d_m} c_m (V_{a_m} + v_{a_m}) \right) \Delta r_m \quad (2)$$

with the subscript m indicating each radial segment of the SRV. To maximize the thrust, the partial derivative of T_V with respect to the circulation distribution is then set to zero:

$$\frac{\partial T_V}{\partial \Gamma_m} = 0 \quad (3)$$

where the derivative is given by:

$$\begin{aligned} \frac{\partial T_V}{\partial \Gamma_m} &= (V_{t_m} + v_{t_m}) \Delta r_m + \sum_i \frac{\partial v_{t_i}}{\partial \Gamma_m} \Gamma_i \Delta r_i \\ &\quad - \sum_i \frac{1}{2} \frac{\partial V_i^*}{\partial \Gamma_m} C_{d_i} c_i (V_{a_i} + v_{a_i}) \Delta r_i \\ &\quad - \sum_i \frac{1}{2} V_i^* \frac{\partial (C_{d_i} \cdot c_i)}{\partial \Gamma_m} (V_{a_i} + v_{a_i}) \Delta r_i \\ &\quad - \sum_i \frac{1}{2} V_i^* C_{d_i} c_i \frac{\partial v_{a_i}}{\partial \Gamma_m} \Delta r_i \end{aligned} \quad (4)$$

The partial derivatives of the induced tangential and axial velocities with respect to the circulation of the horseshoe vortex, called “induction factors,” are computed based on the analytical equations derived by Wrench [28] for constant-pitch helical horseshoe vortices. Moreover, the sectional drag coefficient C_d and the chord length c are prescribed with a constant distribution along the radius ($C_d = 0.01$ and $c = c_r$). It was verified that both the magnitude and the form of the C_d and c distributions have a negligible effect on the circulation distribution obtained by solving Eq. (3), as also found by Epps and Kimball [27]. Therefore, the three terms on the right hand side of Eq. (4) containing $(C_d \cdot c)$ can be neglected and the vane optimization with respect to the drag component is performed in a separate subsequent step. In this way, a non-linear system of equations is formed which can be solved by Newton’s method. In the optimization of the vane geometry, no feedback of the SRVs to the propeller is taken into account. Hence, in this formulation, $\{\Gamma, v_a, v_t\}$ are taken as the vector of unknowns updated and solved by the Newton solver.

3. Airfoil Design of SRV Sections

Having determined the optimal circulation distribution using the lifting-line approach described above, the airfoil shape is designed and optimized to minimize the drag of the SRVs while maintaining the desired circulation distribution. On each vane section, with the constraint of the circulation magnitude, the drag term $(C_d \cdot c)$ is set as the objective function to be minimized. Airfoil profiles may be considered as made up of thickness profile forms disposed about a mean line. As discussed in Ref. [29], the airfoil thickness is of particular importance from a structural standpoint. The mean line form is also important because it determines some of the most important aerodynamic properties of the airfoil section, for example, the angle of zero lift, the pitching moment characteristics, and the stall behavior. To guarantee an airfoil design that complies with acceptable aerodynamics performance and structural characteristics, the airfoil geometry was parameterized using five variables: the maximum thickness t , chordwise position of maximum thickness t_p ,

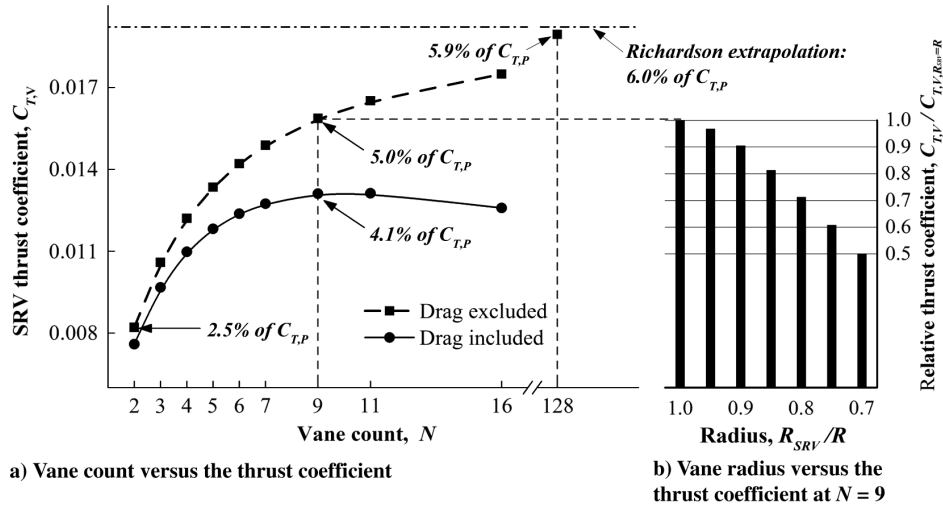


Fig. 6 Parametric study of SRV design at $J = 0.6$ and $C_T = 0.32$.

maximum camber h , chordwise position of maximum camber h_p , and chord length c .

During the periodic interaction with the propeller blade wake, the velocity deficit in axial direction as well as the velocity increase in tangential direction leads to a sudden increase in angle of attack of the SRV section [17,18]. This leads to strong periodic variations in angle of attack, making it important to have a large stall margin for the SRV airfoils. A robust optimization was used and two operating conditions were chosen: the design point at which the design lift coefficient is achieved and the stall angle of the profile (i.e., the angle of attack at maximum lift coefficient). Given a weight factor ω_1 for the drag term at stall and another weight factor ω_2 for the stall margin, the objective function F for the airfoil design is defined as:

$$F(t, t_p, h, h_p, c) = \frac{[(c_d \cdot c)_{des.}]_{opt.}}{[(c_d \cdot c)_{des.}]_{ini.}} + \omega_1 \frac{[(c_d \cdot c)_{stall}]_{opt.}}{[(c_d \cdot c)_{stall}]_{ini.}} - \omega_2 \frac{[(\alpha_{stall} - \alpha_{des.})]_{opt.}}{[(\alpha_{stall} - \alpha_{des.})]_{ini.}} \quad (5)$$

where the subscript *ini.* denotes the initial status and *opt.* the optimized results. The weight factor ω_1 and ω_2 can be chosen based on the magnitude of the inflow angle variation of individual SRV sections. In this study, both were set to 0.5. A minimum relative thickness t/c of 2% was taken as lowest limit for manufacturing. Initial cases were randomly sampled in the design space at the beginning of the optimization loop. A pattern search algorithm was used to perform the optimization, leading to fast convergence. The airfoil performance was determined with XFOIL [30]. The corresponding Reynolds number was calculated based on the local flow parameters, where the velocity term included both the inflow velocities and the induced velocities.

B. Parametric Study of Key SRV Design Parameters

The impact of the vane count and radius on the thrust production by the SRVs was studied by performing parametric studies in which both variables were varied systematically. For each variation, an optimized design was generated using the approach defined in Sec. II.A.

1. Optimal SRV Count

As discussed in Sec. II.A.2, the thrust produced by the SRVs is the result of the axial component of the lift and drag acting on them. It can be expected that by increasing the number of vanes, more residual swirl in the propeller slipstream can be recovered due to the increased solidity. The theoretical maximum in terms of thrust production can be found when the vane count goes to infinity. However, at the same time the drag of the SRVs also increases. Therefore, the optimal performance is obtained as a compromise between maximum swirl

recovery and minimum drag on the SRVs. This tradeoff was investigated by computing the SRV performance as a function of the number of vanes, both with and without including the drag term in the computations. The propeller geometry and operating conditions were the same as introduced before, and the corresponding results are shown in Fig. 6a. Within the no-drag assumption, the thrust increases asymptotically with the vane count, from 2.5% of the propeller thrust with 2 vanes up to 5.9% with 128 vanes. The asymptotic value of the SRV thrust coefficient was estimated by Richardson extrapolation using the computed results for $N = 2, 16,$ and 128 . With the refinement ratio $q = 8$ and the order of convergence $p = 0.892$, the asymptote of $C_{T,V}$ was estimated to be 6% of the propeller thrust. However, the total drag of the SRVs increases approximately linearly with the vane count. Therefore, the optimum number of vanes is obtained when the increment in thrust by addition of an extra vane is compensated by its own drag. As also shown in Fig. 6a, when taking into account the effects of drag, the optimal number of SRVs occurred at $N = 9$, for which the predicted SRV thrust was 4.1% of the propeller thrust. Despite the identification of this optimum vane count, for the validation experiment, only four SRVs were used because of the limited space available in the SRV fairing for the instrumentation of the individual SRVs. It should be noted that the weight penalty resulting from the addition of SRVs is not considered, which should be included when performing the aircraft design equipped with propeller and SRVs.

2. Effect of SRV Cropping

The SRV performance discussed above was obtained under the hypothesis that the radius of the SRVs is the same as that of the propeller. However, as seen in earlier research on CRORs [10], when the second blade row has the same radius as that of the first row, the tip vortices from the first rotor periodically impinge on the leading edge of the second rotor. The resulting unsteady loading leads to an elevated noise level as well as structural vibrations. Therefore, the characterization of the SRV performance as a function of the vane radius is important during the definition of the optimal SRV design, because with decreasing vane radius, less swirl can be recovered by the SRVs. The effect of the SRV radius on the thrust was studied by systematically varying the SRV radius for a fixed vane count of nine and without including the drag term. The results are depicted in Fig. 6b. When the radius is reduced to $0.95R$, 97% of the thrust generated by the uncropped SRVs ($R_{SRV} = R$) is obtained. From this point onward, the thrust coefficient of the SRVs linearly decreases with reduction of the radius, down to 50% of the thrust of uncropped SRVs for the case of an SRV radius of 0.7 times the propeller radius. For the validation experiment, the SRV radius was kept equal to the propeller radius to maximize the thrust contribution of the SRVs, accepting the potential associated noise penalty.

C. Design of SRVs for Validation Experiment

The design method outlined in Sec. II.A was applied to define the shape of the SRVs used for the validation experiment. As mentioned before, a vane count of four was selected, with an SRV radius equal to the radius of the propeller. The vanes were discretized into 20 lifting segments. The resulting optimal circulation distribution is shown in Fig. 7a, together with the distribution of the sectional pitch angle.

Following the steps shown in Fig. 1, after having determined the optimal circulation distribution from the lifting-line method, the airfoil sections need to be designed to achieve minimum drag on the vanes. In the wind-tunnel test, the typical Reynolds number on the vane sections was on the order of 10^5 , at which serious deterioration of the lift and drag may occur due to the laminar separation bubbles [31,32]. On the other hand, the inflow of the SRVs is highly turbulent because of the presence of the propeller upstream of it. In a tractor-propeller configuration, the boundary layer on the part of the wing immersed in the propeller slipstream alternates between laminar and turbulent states, due to the periodic perturbation caused by the passages of the viscous wakes of the propeller blades [33,34]. The SRVs would experience a similar cyclic state change in the boundary layer, promoting transition on the vanes. Before the test, it was not known which of these two effects would dominate. Therefore, it was decided to use forced transition in the airfoil design process, assuming an instantaneous transition to turbulence without accounting for transition device drag. During the airfoil optimization, an optimum chordwise transition position of $z/c = 0.6$ was found to result in the most efficient suppression of the laminar separation bubble and thus minimum drag on the vane section at midradius. Therefore, this setting was implemented for all vane sections. The implications of this choice will be further discussed in Sec. III.C.

Following the design procedure described in Sec. II.A.3, the vane planform was obtained by airfoil optimization performed in two steps. First, individual optimizations were performed to minimize drag at four representative sections: the root section ($r/R = 0.32$),

the section at maximum circulation ($r/R = 0.56$), the tip section ($r/R = 1.00$), and the section between the point of maximum circulation and the tip ($r/R = 0.78$). The resulting optimized airfoil shapes at these sections were used as starting condition for the overall vane planform optimization, with the objective to minimize the total drag of the vane (thus also including the drag at the intermediate stations). The design parameters of the airfoils at the intermediate sections were obtained by interpolation with a piecewise cubic Hermite polynomial. The local angle of attack on each vane section was also determined during the airfoil design process. By adding the local angle of attack to the inflow angle obtained from the lifting-line analysis, the pitch angle was determined and the twist distribution was obtained.

The final geometry characteristics of the airfoils are depicted in Fig. 7b. The airfoils feature a forward maximum thickness position and a backward maximum camber position, which creates a negative pressure plateau on the front part on the suction side as shown in Fig. 8. This front-loaded type of distribution tends to enhance the thrust production from the vanes because only the axial component of aerodynamic forces contributes to the SRV performance.

III. Experimental Validation

A. Experimental Setup

Experiments were conducted with the designed SRVs and the propeller model described in Sec. II.A.1 in a low-speed open-jet wind tunnel at Delft University of Technology. The octagonal test section of the tunnel has a width and height of 2.85 m and a contraction ratio of 3:1. A honey comb flow rectifier along with five screens ensures a straight flow with relatively low turbulence level of about 0.5%, and a maximum flow speed of 29 m/s. The propeller axis is oriented parallel to the centerline of the wind tunnel so that the whole setup is placed at zero angle of attack. The model placed in front of the open jet is shown in Fig. 9.

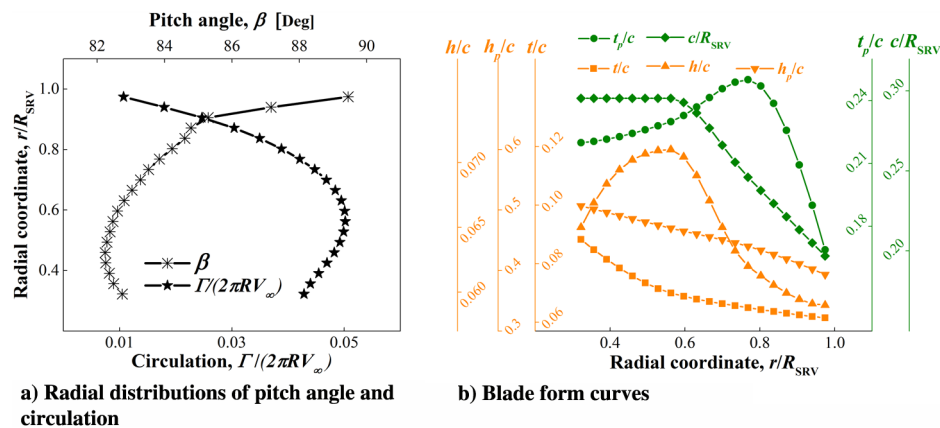


Fig. 7 Blade form curves of SRVs designed with vane count N of 4.

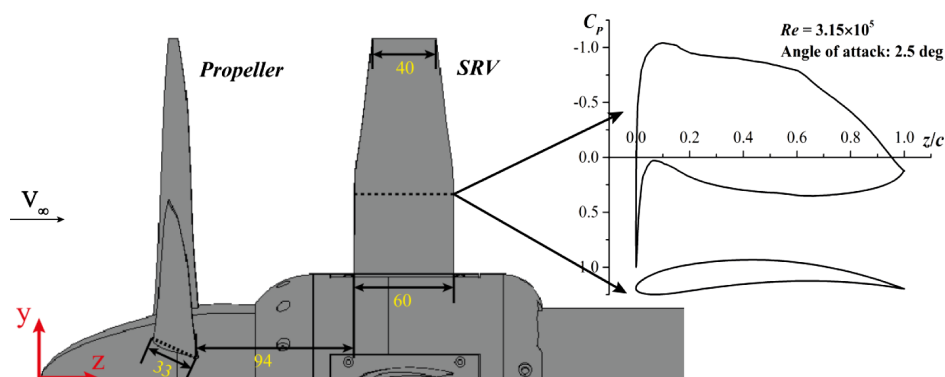


Fig. 8 Sketch of the propeller, the designed SRVs, and the coordinate system (dimensions in millimeters).

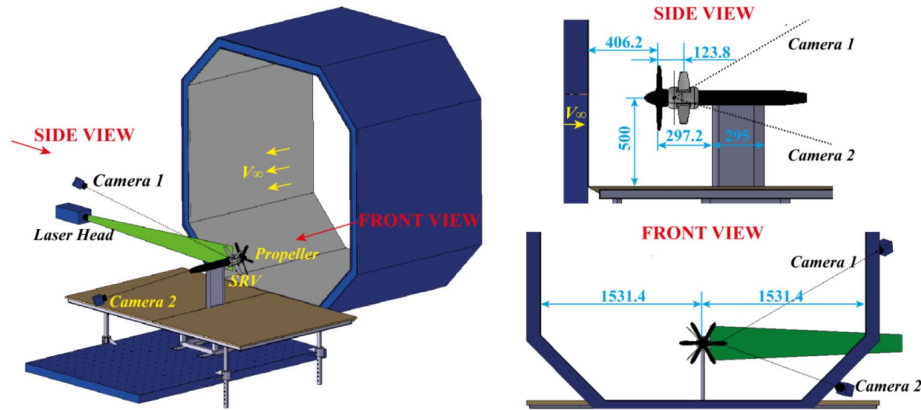


Fig. 9 Sketch of the experimental setup in the wind tunnel including a sketch of the PIV measurement setup (dimensions in millimeters).

The propeller was driven by a Tech Development Inc. 1999 pneumatic motor, and featured an integrated six-component rotating shaft balance (RSB) to measure the propeller forces and moments during operation. A detailed description of the RSB is provided in [35]. The RSB data were acquired at a sampling rate of 10 kHz, and subsequently phase-averaged based on a simultaneously recorded one-per-revolution trigger signal. In this paper, only the time-averaged out-of-plane components of the propeller loading (thrust and torque) are discussed. The RSB measurements were taken for the configurations with and without the SRVs installed to assess the upstream effect of the SRVs on the propeller loading. The uncertainty of the RSB data was reduced by performing advance ratio sweeps five times for each configuration, after which curve fits were generated to model the thrust and torque response of the propeller as a function of the advance ratio.

A second measurement of the disk loading was obtained by taking single-point Pitot pressure measurements at $0.62c_r$ behind the propeller at a radial position of $0.75R$. The Pitot probe had an outer diameter of 2.5 mm and inner diameter of 1.3 mm. Analysis of the results obtained from the RANS simulation indicates that the maximum crossflow angle to the probe was less than 20 deg. As indicated in Ref. [36], at such angles the measurement error remains within 1% of the dynamic pressure. Therefore, no corrections were applied for the misalignment of the Pitot probe with the local velocity direction. The pressure measurements were obtained by a Mensor® differential digital pressure gauge, with the ambient pressure outside the airstream taken as reference pressure. The sampling frequency was set to 10 Hz in order to obtain a statistically converged dataset by averaging over 15 s of measurement time.

A fairing was required to house the instrumentation and support structure of the SRVs. This fairing should be considered as an artifact of the test setup, which would not be present in a full-scale propeller-SRV configuration. The fairing had an outer radius of 63 mm (31% of propeller radius) and was mounted directly on the nacelle. A sliding system for each SRV was positioned inside the fairing, providing freedom to axial translation while constraining translation and rotation in the other five directions. The sliding system consisted of a steel track that was fixed to the fairing and two linear sliding units with two sets of linear ball bearings each. Each SRV was mounted on two sliding units; a load cell with maximum capacity of 20 N was installed on each track in front of the vane measuring the axial thrust per vane. The sampling frequency of the load-cell measurements was set at 50 kHz for a total measurement time of 15 s corresponding to about 1800 propeller revolutions at a propeller rotation frequency of 120 Hz at $J = 0.6$. It should be noted that the nonzero adhesion force of unknown magnitude of the sliding system always needs to be exceeded whenever the vanes are producing either thrust or drag. In this respect, the load-cell readings corresponded to the net SRV thrust minus the adhesion force, thus indicating the lower bound of the thrust that the SRVs produced. Forced transition was achieved on the SRVs by implementing a zigzag strip on the suction side. The strips had a thickness of 0.2 mm and sweep angle of 90 deg, and were located at $z/c = 0.5$ to guarantee a successful transition at 60% of the

vane chord. Tests were performed both with and without transition strips to verify whether there is a need for forced transition during the airfoil design step.

Measurements of the flowfield surrounding the SRVs were taken using stereoscopic particle image velocimetry. A Quantel® Evergreen Nd: YAG laser with a maximum pulse energy of 200 mJ was used to illuminate the particles, forming a laser sheet of about 2 mm thickness. Two LaVision Imager Pro LX cameras were used, with a resolution of 4870×3246 pixel and a pixel pitch of $7.4 \mu\text{m}/\text{pixel}$. A lens with focal length of 200 mm was used for the lower camera, while a larger focal length (300 mm) was adopted for the upper camera to compensate for the longer distance to the measurement plane (Fig. 9). The field of view spanned around 225×150 mm, resulting in a digital resolution of 21.6 pixel/mm. The measurement planes were located at $0.4c_r$ upstream and downstream of the SRVs. A SAFEX® Twin Fog Double Power smoke generator was used to produce seeding particles with an average diameter of $1 \mu\text{m}$. For each test case, a total number of 1000 statistically independent image pairs were acquired and the resulting vector fields were averaged such that the measurements represent the time-averaged flowfield. The final interrogation window size of 48×48 pixel with 75% overlap resulted in a spatial resolution of 0.55 mm.

B. Uncertainty Analysis of Experimental Measurements

The calibration uncertainty of the RSB data for the static out-of-plane components (which corresponds to the propeller thrust and torque) is smaller than 0.25% of full range [35], that is, 0.875 and 0.075 N · m, respectively. With an assumption of linear uncertainty propagation, the uncertainties of thrust and torque coefficients are calculated to be 0.0019 and 0.00039 at an advance ratio $J = 0.6$. This estimate does not include potential additional calibration errors due to rotational effects and bias errors during the measurements. The Pitot pressure measurement has an uncertainty of 1.5 Pa, corresponding to an uncertainty of the pressure coefficient of 0.0029 at a freestream velocity of 29 m/s.

The rated accuracy of the load cell used to measure the SRV thrust is 0.1% of full range (0.02 N), resulting in an uncertainty of thrust coefficient of 4.2×10^{-5} at an advance ratio J of 0.6. As mentioned in Sec. III.A, there are adhesion forces acting on the sliding units of the measurement system. These adhesion forces are proportional to the loading of the vanes. Considering the fact that the gravitational force of the vanes plays a different role for the vanes at different azimuthal positions (supporting or opposing the aerodynamic side force and torque), the adhesion forces on the vanes are different. Thus, the main uncertainty of the load-cell measurements comes from the uncertainty of the adhesion forces of the sliding units. The resulting uncertainty can be obtained by calculating the standard deviation of the thrust measured from different vanes, which will be presented when discussing the SRV performance.

The uncertainty quantification of PIV results was performed based on correlation statistics [37]. This method uses the differences between two interrogation windows. The calculated displacement field is used to map

back the second image onto the first one. By calculating the position of the particle in each interrogation window, the residual disparity in the position of matching particles gives an estimate of the measurement uncertainty. The uncertainty of the instantaneous velocity components is 0.73 m/s for the in-plane components and 0.85 m/s for the out-of-plane component (approximately 3% of the freestream velocity). Because vector fields were averaged from the 1000 samples, the uncertainty of the time-averaged results is reduced after averaging.

C. Characterization of Propulsive Performance of the SRVs

The total thrust coefficient of the SRVs obtained from the load-cell measurements is depicted as a function of propeller advance ratio in Fig. 10. It should be mentioned again that the experimental results only represent the *minimum* thrust generated by the SRVs, as discussed in Sec. III.A. The measured SRV thrust increased gradually from 1.5% of the propeller thrust at the low propeller loading condition of $J = 1.0$ up to 2.6% of the propeller thrust at the highest loading condition of $J = 0.55$. At the design condition of $J = 0.6$, an SRV thrust of 2.6% of the propeller thrust was measured in the experiment for the SRVs with free transition, compared with 3.4% predicted by lifting-line theory. With transition strip installed, only 2.4% of the propeller thrust was produced at the design point. This could be the result of the added drag due to the tripping device. The absence of the performance penalty expected for the untripped configuration due to laminar separation could be due to the turbulent perturbations upstream of the vanes caused by the periodic passage of the propeller blade wakes, as discussed before in Sec. II.C. No evidence was found in the present experiments of the possible performance penalty through relaminarization and consequently the formation of a separation bubble on the SRVs, as reported by Renoud and Howard [34] for the nacelle of a propeller. The passage of turbulent segments on the vane's suction side may have stabilized the transitional and turbulent boundary layers and eliminated the possible laminar separation. Thus, the addition of the transition strip did not contribute to the attenuation of the total drag but only caused extra device drag.

It is an intrinsic characteristic of a propeller that the slipstream exhibits a strong but periodic unsteadiness, resulting from the passages of the blade wakes and tip vortices. Consequently, the propulsive performance of the SRVs demonstrates severe fluctuations corresponding to the periodic inflow conditions. As an example, the unsteadiness of $C_{T,V}$ at $J = 0.6$ from one of the vanes without transition strip is shown in Fig. 11 within one propeller revolution. With the sampling frequency of the load cell at 50 kHz and propeller rotation frequency at 120 Hz, the measurements have a temporal resolution of 0.9 deg. At each propeller phase angle, results were phase-averaged over the 1800 samples,

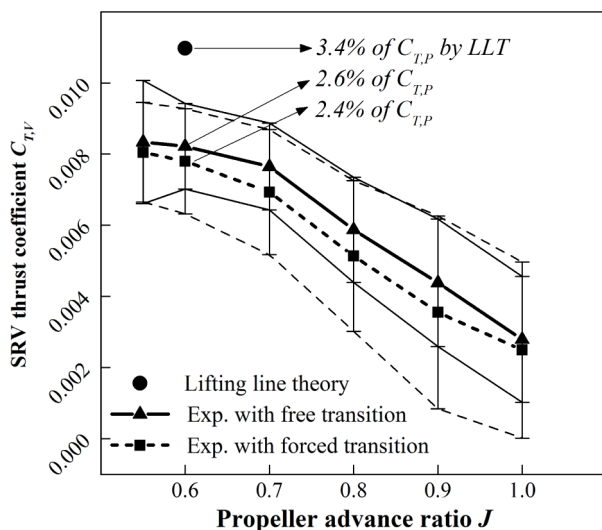


Fig. 10 Time-averaged propulsive performance of the SRVs measured with the load cells. LLT denotes the result computed with lifting-line theory.

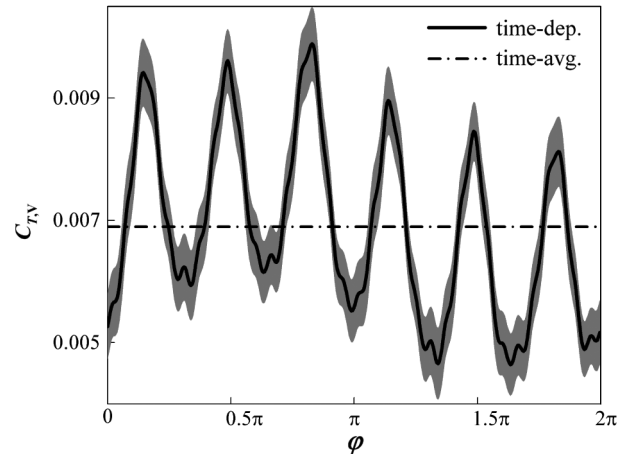


Fig. 11 Unsteady propulsive performance of one SRV at $J = 0.6$ without transition strip measured using the load cell. The 95% confidence level is indicated by the gray area.

as shown as the solid line in Fig. 11. Assuming the load cell reading at each propeller phase angle to have a normal distribution, the confidence interval with 95% confidence level would lie within 1.96 times the standard deviation around the mean value. This is depicted as the gray area in Fig. 11. Six peaks are observed in the time-dependent thrust coefficient. These are the direct result of the periodic impingement of the wakes and tip vortices of the six propeller blades on the SRVs as discussed in Ref. [17]. In the wake of the propeller blade, the velocity deficit in axial direction as well as the velocity increase in tangential direction leads to a sudden increase in angle of attack and subsequently the lift and drag experienced by the downstream SRVs. As discussed previously, the thrust of the SRVs originates from the axial component of lift and drag exerted on the vanes. Therefore, the increment in magnitude of lift and drag leads to the increment in thrust. More important, the sectional inflow direction is tilted by the change of the velocity components. Given a certain radial position, with higher tangential velocity and lower axial velocity, the sectional lift is tilted into the axial direction and the sectional drag is tilted more into the normal direction, leading to an increase of the thrust component. In the end, the change in magnitude as well as direction of the sectional lift and drag leads to a spike in the thrust coefficient every time the propeller wake passes by an SRV.

D. Characterization of Propulsive Performance of the Propeller

The propulsive performance of the propeller was obtained from the RSB measurements, of which the results are shown in Fig. 12. The propeller characteristics with and without the addition of the downstream SRVs are compared in the top part of the figure. Each symbol represents a data point and the overall trend was estimated by curve fitting with a fourth-order polynomial. In terms of the efficiency, the fitting curve was computed from those of C_T and C_Q following the definition of the propeller efficiency. The adjusted R-squares of all fits were greater than 0.9997, which indicates good fits of the data points. The fitting curves for the SRV on and off case almost coincide, which means that the upstream effect of SRVs is negligible. This confirms the assumption made in the design procedure, as discussed in Sec. II.A.1.

The propeller performance obtained from the numerical simulation of the propeller at $J = 0.6$ is also shown in Fig. 12. The numerical results are observed to have a good agreement with the experimental data. Compared with the thrust coefficient of 0.323 measured by the RSB at the design condition, a $C_{T,P}$ of 0.322 was estimated by the simulation, corresponding to a relative error of 0.3%.

Considering the combination of propeller and SRVs as a propulsion system, the performance was compared with that of the isolated propeller as shown in the bottom part of Fig. 12. The black and blue columns, which represent the cases for the propeller with SRVs off and on, respectively, were taken from the fitting curves at each advance ratio. After adding the SRV thrust coefficient $C_{T,V}$ from

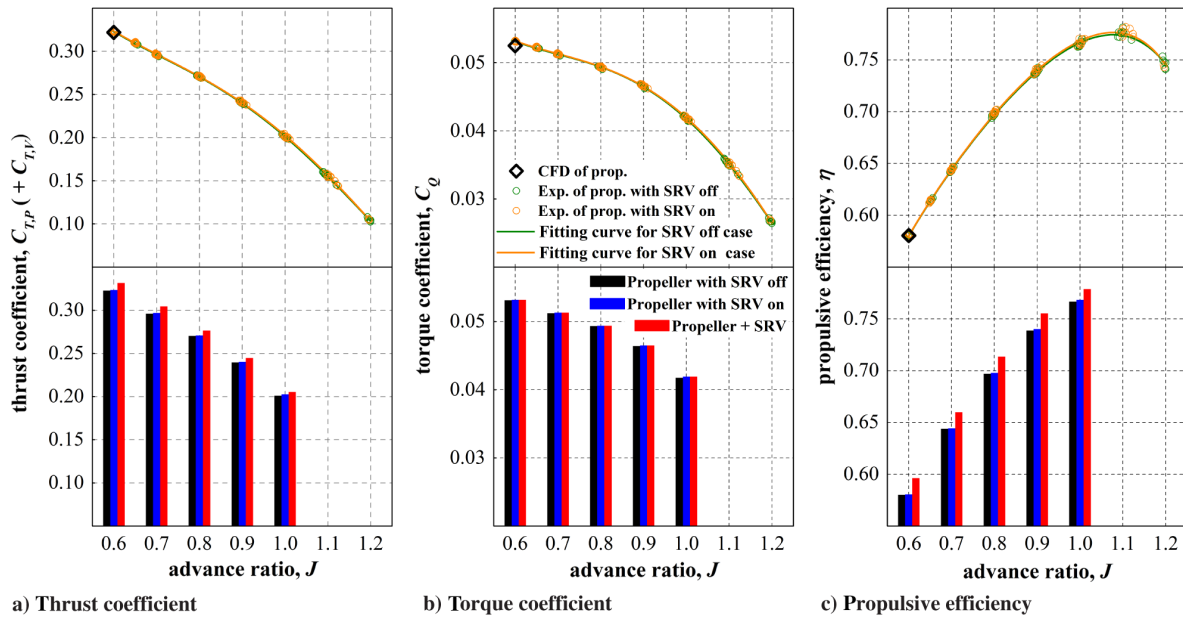


Fig. 12 Propulsive performance of the propulsion system with and without the SRVs installed.

Fig. 10 to the measured propeller thrust coefficient, the red column in Fig. 12a represents the thrust of the propulsion system. Because the vanes do not require any power input, the torque coefficient of the system was the same as that of the propeller (with SRVs installed), as shown in Fig. 12b. The resulting propulsive efficiency was then computed at each advance ratio, as depicted in Fig. 12c. A prevalent feature of the efficiency plot is that the system efficiency has improved at all advance ratios by installation of the SRVs. At the design condition of $J = 0.6$, the propulsive efficiency increased from 0.581 to 0.596, while at $J = 0.7$, the efficiency went up from 0.644 until 0.660, and at $J = 1.0$, the efficiency improved from 0.767 to 0.779. However, as mentioned in Sec. II.B.1, these numbers do not account for the weight penalty resulting from the addition of SRVs. An aircraft design study would need to be performed to estimate the performance benefit at airplane level, which was considered out of the scope of the present paper.

The power exerted by the propeller on the air results in a rise in total temperature, total pressure, and angular momentum in the slipstream. Besides the shaft forces discussed above, the dynamic pressure behind the propeller is also indicative of the propeller loading. Therefore, measurements of the dynamic pressure were taken at $1.5c_r$ behind the propeller at an advance ratio of $J = 0.6$ and a radial coordinate of $r/R = 0.75$. The resulting pressure coefficient was 4.147 ± 0.003 with SRVs installed and 4.157 ± 0.001 without SRVs, corresponding to a change of only 0.24%. This once more confirms that the disturbance of the propeller inflow due to the presence of the SRVs is negligible, which can be explained from the relatively large spatial separation between the propeller and the SRVs, and the low loading and solidity of the vanes [18].

E. Flowfield Description by PIV Measurements

The input velocities from the RANS simulation of the propeller were validated by PIV measurements on vertical planes positioned at $0.4c_r$ upstream and downstream of the location of the SRVs, for the configuration without SRVs installed. Figure 13 compares the circumferentially averaged axial and tangential velocity profiles as measured during the experiment with the results obtained from the RANS simulation. The axial positions of the measurement planes are indicated by the red dashed lines. In the upstream plane, reasonable agreement is observed between computed and measured data, both in terms of the general shape of the velocity profile and the magnitude of the tangential and axial velocities. The maximum difference between the experimental and numerical results was 1.1 m/s, corresponding

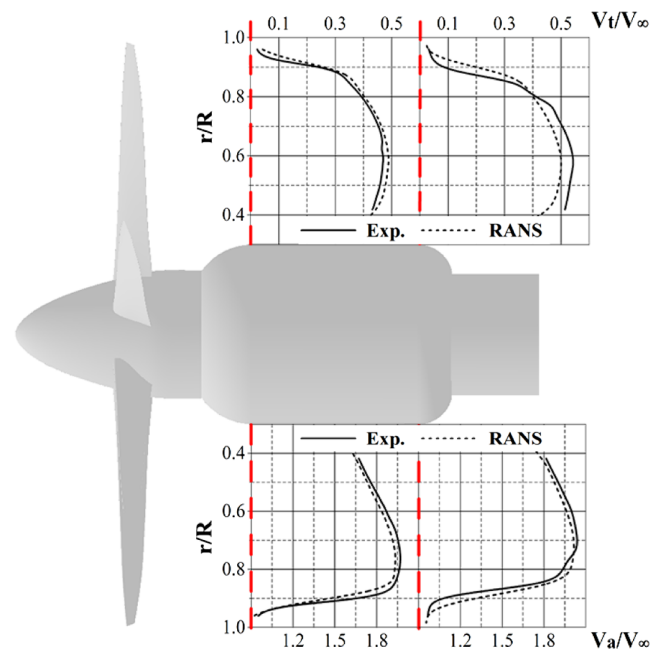


Fig. 13 Validation of the input velocities from RANS simulation of the propeller at $J = 0.6$.

to 3.8% of the freestream velocity. In the downstream plane, this observation also applies for the axial velocity, but in terms of the circumferential velocity a slightly larger difference is visible. This is attributed to the coarser mesh density in this plane, because the downstream plane is outside of the dense grid region arranged around the SRVs (Fig. 3).

The PIV measurements also quantified the swirl recovery achieved by the SRVs, as shown in Fig. 14. In the plane upstream of the SRVs, no obvious change was observed after installation of the SRVs. At this position, the flowfield can be affected only by the vanes due to potential-flow effects, but the plane was far enough away from the SRVs to make the changes to the flowfield insignificant. From this observation, it can also be expected that the installation of the SRVs has negligible influence on the propeller performance, which is consistent with the measurement data discussed in Sec. III.D. In the plane downstream of the SRVs, the swirl was reduced by installation

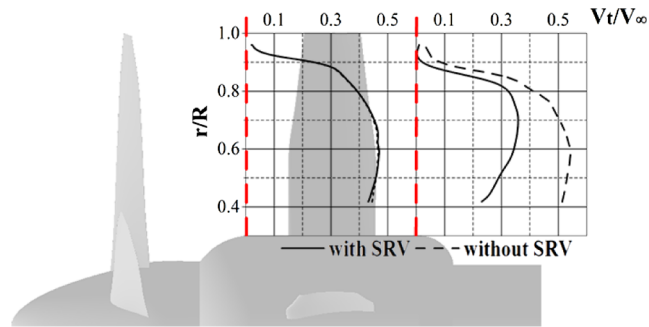


Fig. 14 Quantification of swirl recovery by SRVs from PIV measurements at $J = 0.6$.

of the SRVs, with the amount of swirl recovery increasing toward the nacelle. When integrated along the radius, 42% of the angular momentum was recovered by the SRVs.

IV. Conclusions

This paper has developed a hybrid framework for swirl-recovery vane (SRV) design based on a lifting-line model. The design procedure consists of three steps. First, the inflow velocities are prescribed, as obtained from a numerical simulation of the isolated propeller or from an experiment. Second, the optimum loading distribution of the SRVs is determined by lifting-line theory with the objective of maximum SRV thrust. Third, an airfoil design routine is performed to optimize the SRV airfoil sections and the planform geometry. The design method allows for a fast turnaround time and is thus suitable for system-level design and parameter studies.

As a test example, a set of SRVs was designed for a six-bladed propeller at a high propeller loading condition ($C_{T,P} = 0.322$) with a Reynolds number of 7.9×10^5 relative to the propeller diameter and freestream velocity of 29 m/s. The flowfield around the propeller was simulated with a RANS solver, after which the resulting velocity fields in the propeller slipstream were used as input to the SRV design procedure. A parametric study was performed of the SRV performance as a function of the vane count and radius. It was concluded that the maximum SRV thrust could be obtained with a vane count of 9 and vane radius equal to that of the propeller. For this case, it was estimated that 4.1% of the propeller thrust could be produced by the SRVs.

To validate the design routine, an experiment was performed with a propeller and SRVs in a low-speed open-jet wind tunnel. Because of practical constraints, a vane count of four was chosen instead of the identified optimum of nine, and a new design was generated for this vane count. The thrust generated by the SRVs was measured with load cells mounted on sliding bearings. At the design point, the SRVs generated a thrust of 2.6% of that of the propeller, which is smaller compared with the prediction of 3.4% by the lifting-line method. Because the installation of the SRVs does not increase the required power input, this indicates the same amount of improvement in the system propulsive efficiency. The thrust coefficient of the SRVs showed an approximately linear relation with the propeller advance ratio, diminishing to 1.5% of the propeller thrust at a cruise condition of $J = 1.0$.

The propeller performance was characterized by balance measurements. The measurements showed that the upstream effect of the SRVs on the propeller performance was negligible. Because the SRVs provided thrust at all the measured advance ratios ($J = 0.6$ up to 1.0), and did not require any extra power input, the propulsive efficiency of the system (propeller + SRVs) improved accordingly, for all flight phases considered.

Acknowledgments

The authors would like to thank the China Scholarship Council for the partial financial support of the study, and Henk-Jan Siemer, Nico van Beek, Frits Donker Duyvis, Peter Duyndam, Dennis Bruikman, and Stefan Bernardy for their assistance during the experiments at Delft University of Technology's Open Jet Facility.

References

- [1] International Civil Aviation Organization, "ICAO Environmental Report 2016," 2016. <http://www.icao.int/environmental-protection/Documents/ICAO%20Environmental%20Report%202016.pdf> [accessed 07 Sept. 2017].
- [2] Mikkelsen, D. C., Mitchell, G. A., and Bober, L. J., "Summary of Recent NASA Propeller Research," NASA TM-83733, Oct. 1984.
- [3] Stürmer, A., "Unsteady CFD Simulations of Contra-Rotating Propeller Propulsion Systems," 44th AIAA/ASME/SAE/ASEE Joint Propulsion Conference & Exhibit, AIAA Paper 2008-5218, July 2008.
- [4] Stürmer, A., and Yin, J., "Installation Impact on Pusher CROR Engine Low Speed Performance and Noise Emission Characteristics," *International Journal of Engineering Systems Modelling and Simulation*, Vol. 4, Nos. 1–2, 2012, pp. 59–68. doi:10.1504/IJESMS.2012.044844
- [5] Stürmer, A., and Yin, J., "Pylon Trailing Edge Blowing for the Control of CROR Unsteady Blade Loads," *New Results in Numerical and Experimental Fluid Mechanics VIII: Contributions to the 17th STAB/DGLR Symposium*, Berlin, 2010, edited by A. Dillmann, G. Heller, H.-P. Kreplin, W. Nitsche, and I. Peltzer, Vol. 121, Notes on Numerical Fluid Mechanics and Multidisciplinary Design, Springer, Berlin, 2013, pp. 715–722. doi:10.1007/978-3-642-35680-3_85
- [6] Akkermans, R. A. D., Stürmer, A., and Delfs, J. W., "Active Flow Control for Interaction Noise Reduction of Contra-Rotating Open Rotors," *AIAA Journal*, Vol. 54, No. 4, 2016, pp. 1413–1423. doi:10.2514/1.J053756
- [7] Strack, W. C., Knip, G., Weisbrich, A. L., Godston, J., and Bradley, E., "Technology and Benefits of Aircraft Counter Rotation Propellers," NASA TM-82983, Jan. 1981.
- [8] Dominy, J., and Midgley, R. A., "A Transmission for the Contra-Rotating Prop-Fan Powerplant," *AIAA/SAE/ASME 20th Joint Propulsion Conference*, AIAA Paper 1984-1196, June 1984.
- [9] Godston, J., and Mike, F. J., "Evaluation of Single and Counter Rotation Gearboxes for Propulsion Systems," *AIAA/SAE/ASME 20th Joint Propulsion Conference*, AIAA Paper 1984-1195, June 1984.
- [10] Stürmer, A., Marquez Gutierrez, C. O., Roosenboom, E. W. M., Schröder, A., Geisler, R., Pallek, D., Agocs, J., and Neitzke, K.-P., "Experimental and Numerical Investigation of a Contra Rotating Open-Rotor Flowfield," *Journal of Aircraft*, Vol. 49, No. 6, 2012, pp. 1868–1877. doi:10.2514/1.C031698
- [11] Blandeau, V. P., and Joseph, P. F., "Broadband Noise due to Rotor-Wake/Rotor Interaction in Contra-Rotating Open Rotors," *AIAA Journal*, Vol. 48, No. 11, 2010, pp. 2674–2686. doi:10.2514/1.J050566
- [12] Miller, C. J., "Euler Analysis of a Swirl Recovery Vane Design for Use with an Advanced Single-Rotation Propfan," *AIAA/SAE/ASME/ASEE 24th Joint Propulsion Conference*, AIAA Paper 1988-3152, July 1988.
- [13] Gazzaniga, J. A., and Rose, G. E., "Wind Tunnel Performance Results of Swirl Recovery Vanes as Tested with an Advanced High Speed Propeller," *AIAA/SAE/ASME/ASEE 28th Joint Propulsion Conference and Exhibit*, AIAA Paper 1992-3770, July 1992.
- [14] Dittmar, J. H., and Hall, D. G., "The Effect of Swirl Recovery Vanes on the Cruise Noise of an Advanced Propeller," *13th Aeroacoustics Conference*, AIAA Paper 1990-3932, Oct. 1990.
- [15] Wang, Y., Li, Q., Eitelberg, G., Veldhuis, L. L. M., and Kotsonis, M., "Design and Numerical Investigation of Swirl Recovery Vanes for the Fokker 29 Propeller," *Chinese Journal of Aeronautics*, Vol. 27, No. 5, 2014, pp. 1128–1136. doi:10.1016/j.cja.2014.03.009
- [16] Stokkermans, T. C. A., van Arnhem, N., and Veldhuis, L. L. M., "Mitigation of Propeller Kinetic Energy Losses with Boundary Layer Ingestion and Swirl Recovery Vanes," *Proceedings of the 2016 Applied Aerodynamics Conference*, Royal Aeronautical Soc., London, U.K., 2016.
- [17] Li, Q., Wang, Y., and Eitelberg, G., "An Investigation of Tip Vortices Unsteady Interaction for Fokker 29 Propeller with Swirl Recovery Vane," *Chinese Journal of Aeronautics*, Vol. 29, No. 1, 2016, pp. 117–128. doi:10.1016/j.cja.2015.12.004
- [18] Sinnige, T., Stokkermans, T. C. A., Ragni, D., Eitelberg, G., and Veldhuis, L. L. M., "Aerodynamic and Aeroacoustic Performance of a Propeller Propulsion System with Swirl-Recovery Vanes," *Journal of Propulsion and Power*, 2018. doi:10.2514/1.B36877

- [19] Obayashi, S., and Tsukahara, T., "Comparison of Optimization Algorithms for Aerodynamic Shape Design," *AIAA Journal*, Vol. 35, No. 8, 1997, pp. 1413–1415.
doi:10.2514/2.251
- [20] Hildebrand, F. B., "Topics in Higher-Dimensional Calculus," *Advanced Calculus for Applications*, Prentice-Hall, Englewood Cliffs, NJ, 1962, pp. 357–359.
- [21] Coney, W. B., "A Method for the Design of a Class of Optimum Marine Propulsors," Ph.D. Dissertation., Dept. of Ocean Engineering, Massachusetts Inst. of Technology, Cambridge, MA, 1989.
- [22] Ortun, B., Boisard, R., and Gonzalez-Martino, I., "In-Plane Airloads of a Propeller with Inflow Angle: Prediction vs. Experiment," *30th AIAA Applied Aerodynamics Conference*, AIAA Paper 2012-2778, June 2012.
- [23] Lignarolo, L. E. M., Ragni, D., Krishnaswami, C., Chen, Q., Ferreira, C. J., and Van Bussel, G. J. W., "Experimental Analysis of the Wake of a Horizontal-Axis Wind-Turbine Model," *Renewable Energy*, Vol. 70, Oct. 2014, pp. 31–46.
doi:10.1016/j.renene.2014.01.020
- [24] Menter, F. R., "Two-Equation Eddy-Viscosity Turbulence Models for Engineering Applications," *AIAA Journal*, Vol. 32, No. 8, 1994, pp. 1598–1605.
doi:10.2514/3.12149
- [25] Balasubramanian, R., Barrows, S., and Chen, J., "Investigation of Shear-Stress Transport Turbulence Model for Turbomachinery Applications," *46th AIAA Aerospace Sciences Meeting and Exhibit*, AIAA Paper 2008-0566, Jan. 2008.
- [26] Roache, P. J., "Perspective: A Method for Uniform Reporting of Grid Refinement Studies," *Journal of Fluids Engineering*, Vol. 116, No. 3, 1994, pp. 405–413.
doi:10.1115/1.2910291
- [27] Epps, B., and Kimball, R. W., "Unified Rotor Lifting Line Theory," *Journal of Ship Research*, Vol. 57, No. 4, 2013, pp. 181–201.
doi:10.5957/JOSR.57.4.110040
- [28] Wrench, J. W., Jr., "The Calculation of Propeller Induction Factors," Applied Mathematics Lab. TR 1116, David Taylor Model Basin, Feb. 1957.
- [29] Jacobs, E. N., Ward, K. E., and Pinkerton, R. M., "The Characteristics of 78 Related Airfoil Sections from Tests in the Variable-Density Tunnel," NACA TR-460, Jan. 1933.
- [30] Drela, M., "XFoil: An Analysis and Design System for Low Reynolds Number Airfoils," *Low Reynolds Number Aerodynamics*, Springer, Berlin, 1989, pp. 1–12.
- [31] Gopalarathnam, A., Broughton, B. A., McGranahan, B. D., and Selig, M. S., "Design of Low Reynolds Number Airfoils with Trips," *Journal of Aircraft*, Vol. 40, No. 4, 2003, pp. 768–775.
doi:10.2514/2.3157
- [32] Lyon, C. A., Selig, M. S., and Broeren, A. P., "Boundary Layer Trips on Airfoils at Low Reynolds Numbers," *35th Aerospace Sciences Meeting & Exhibit*, AIAA Paper 1997-0511, Jan. 1997.
- [33] Howard, R. M., and Miley, S. J., "Time-Dependent Boundary-Layer Response in a Propeller Slipstream," *Journal of Aircraft*, Vol. 26, No. 9, 1989, pp. 863–869.
doi:10.2514/3.45852
- [34] Renoud, R. W., and Howard, R. M., "Airfoil Boundary-Layer Response to an Unsteady Turbulent Flowfield," *AIAA Journal*, Vol. 28, No. 11, 1990, pp. 1894–1900.
doi:10.2514/3.10496
- [35] Nahuis, R., and Sinnige, T., "Design, Manufacture and Commissioning of a New NLR Six-Component Rotating Shaft Balance for Delft University of Technology," *10th International Symposium on Strain-Gauge Balances*, China Aerodynamics Research and Development Center, Mianyang, China, 2016.
- [36] Gracey, W., "Wind-Tunnel Investigation of a Number of Total-Pressure Tubes at High Angles of Attack-Subsonic, Transonic, and Supersonic Speeds," NACA TR-1303, Jan. 1957.
- [37] Wieneke, B., "PIV Uncertainty Quantification from Correlation Statistics," *Measurement Science and Technology*, Vol. 26, No. 7, 2015, Paper 074002.
doi:10.1088/0957-0233/26/7/074002

F. N. Coton
Associate Editor